

Event Ellipsometer: Event-based Mueller-Matrix Video Imaging - Supplemental Document -

Ryota Maeda^{1,2} Yunseong Moon¹ Seung-Hwan Baek¹

¹POSTECH ²University of Hyogo

In this supplemental document, we provide additional results and details of Event Ellipsometer.

Contents

1. Image Formation	2
1.1. Mueller Matrices of Optical Elements	2
1.2. Time Difference Computation with Refractory Time	2
1.3. QWP Angles	2
2. Reconstruction Method	2
2.1. Spatio-temporal Propagation Pattern	2
3. Hardware Implementation	2
3.1. Part List	2
3.2. Rotation Speed Control	3
3.3. Rotation Angle and Event Time Correspondence	3
3.4. Contrast Threshold Calibration	4
3.5. QWP Offset Angle Calibration	5
4. Additional Results	5
4.1. Ablation Study	5
4.2. Rotation Stability of the Prototype	6
4.3. Comparison with Frame-based Method	7
4.4. Comparison with Single-shot Method	7
4.5. Statistics of Event Rate	8
4.6. Detailed Results with Decomposed Mueller Matrix	8
5. Additional Discussion	9
5.1. Wavelength Dependency	9
5.2. Temporal Artifact in the Mueller-matrix Video	11
5.3. Motion Artifacts	13
5.4. Motor Selection	13

1. Image Formation

1.1. Mueller Matrices of Optical Elements

Mueller matrix of linear polarizer \mathbf{L} and quarter-wave plate \mathbf{Q} with rotation angle θ are represented by as follows [2]:

$$\mathbf{L}(\theta) = \frac{1}{2} \begin{bmatrix} 1 & \cos(2\theta) & \sin(2\theta) & 0 \\ \cos(2\theta) & \cos^2(2\theta) & \sin(2\theta)\cos(2\theta) & 0 \\ \sin(2\theta) & \sin(2\theta)\cos(2\theta) & \sin^2(2\theta) & 0 \\ 0 & 0 & 0 & 0 \end{bmatrix}, \quad (1)$$

$$\mathbf{Q}(\theta) = \begin{bmatrix} 1 & 0 & 0 & 0 \\ 0 & \cos^2(2\theta) & \sin(2\theta)\cos(2\theta) & -\sin(2\theta) \\ 0 & \sin(2\theta)\cos(2\theta) & \sin^2(2\theta) & \cos(2\theta) \\ 0 & \sin(2\theta) & -\cos(2\theta) & 0 \end{bmatrix}. \quad (2)$$

1.2. Time Difference Computation with Refractory Time

The event camera has a refractory time η , during which the sensor is unable to detect intensity changes. To incorporate this time into the reconstruction process, we compute the time differences Δt_k as follows:

$$\Delta t_k = t_{k+1} - t_k - \eta. \quad (3)$$

The refractory time η reduces the time difference and the impact of the refractory time η is negligible when the naive time difference ($t_{k+1} - t_k$) is large but becomes significant for the smaller time difference. We obtained the refractory time value using Metavision SDK¹.

1.3. QWP Angles

As introduced in the main paper, we denoted the QWP angles as $\theta_{1,t} = \omega t + i_1$ and $\theta_{2,t} = 5\omega t + i_2$, and the detailed definition of i_1 and i_2 are defined as follows:

$$i_1 = \phi_{\text{calib1}}, \quad (4)$$

$$i_2 = \phi_{\text{calib2}} - 5\phi_{\text{dynamic},f}, \quad (5)$$

where ϕ_{calib1} and ϕ_{calib2} are fixed offset angles determined in one-time calibration (Section 3.5). $\phi_{\text{dynamic},f}$ denotes the dynamic offset angle between the two QWPs, measured for each frame (Section 3.3).

2. Reconstruction Method

2.1. Spatio-temporal Propagation Pattern

Our spatial-temporal propagation scheme is inspired by the red-black pattern for stereo depth estimation [4], which enables efficient parallel computation. Extending this spatial pattern into the temporal domain, we define a spatio-temporal pattern as illustrated in Figure 1. This pattern preserves simultaneous updates for both red and black pixels, ensuring computational efficiency across spatial and temporal dimensions in video processing.

3. Hardware Implementation

This section describes the details of our hardware implementation.

3.1. Part List

Table 1 shows the parts list of our hardware prototype.

¹ Metavision SDK, <https://docs.prophesee.ai/stable/index.html>

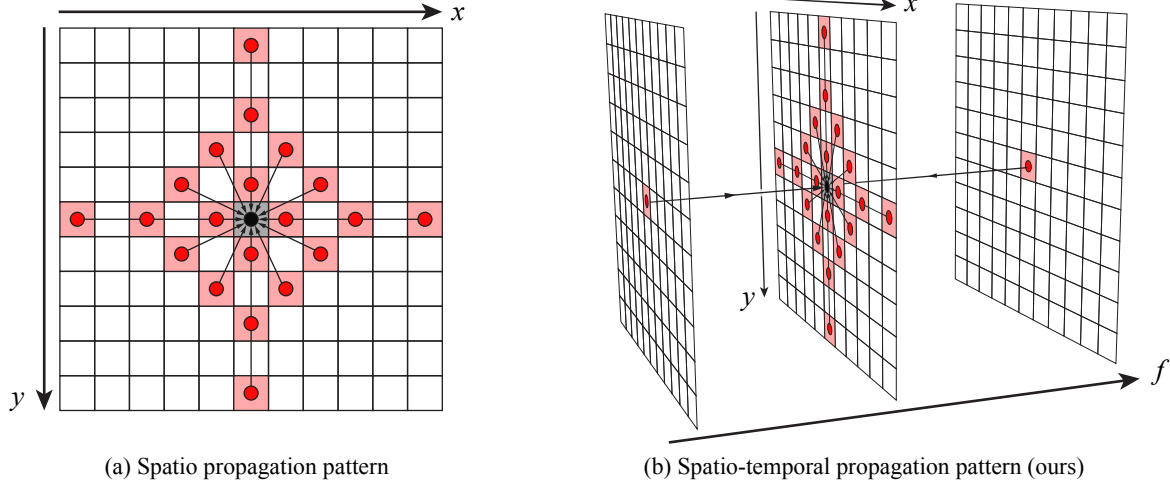


Figure 1. Spatial-temporal propagation pattern. The center pixel (depicted in black) is updated using Mueller-matrix candidates from neighboring pixels (depicted in red). (a) The original red-black propagation pattern, which considers only the spatial axes (x and y) [4]. (b) Our propagation pattern extends this scheme into the temporal axis (f).

Part description	Model name	Quantity
Quarter-wave plate	Edmund Optics WP140HE	2
Linear polarizer	Thorlabs WP25M-VIS	2
Event camera	Prophesee EVK4	1
Lens	8mm F1.4	1
LED light	Thorlabs MCWHLP3	1
LED driver	Thorlabs LEDD1B	1
Microcontroller	Arduino UNO R4	1
Motor	Maxon A-max 19 (249993)	2
Motor driver	Pololu DRV8835	2
Photointerrupter	SHARP GP1S094HCZ0F	2
DC power supply	BK Precision 9111	1

Table 1. Parts list of our hardware prototype.

3.2. Rotation Speed Control

To ensure constant-speed rotation of the QWPs, we implemented a feedback-based control mechanism using the measured rotation speed measured with photointerrupters. Each photointerrupter consists of an LED and a photodetector, which work together with an occluder attached to the motor shaft. This setup detects interruptions in the light path, which are then converted into rotation speed measurements. Based on these measurements, we regulate the motor current through pulse-width modulation (PWM), with the duty cycle controlled by a Proportional-Integral-Derivative (PID) controller. We manually tuned the PID controller parameters to achieve stable rotation.

3.3. Rotation Angle and Event Time Correspondence

To establish the correspondence between the rotation angle and the recorded event time, we utilized the trigger interface feature provided in Prophesee EVKs. This interface allows for the recording of trigger events generated by external hardware signals. Utilizing this functionality, we recorded the interrupted timing from the motor’s encoder and incorporated it into the Mueller-matrix reconstruction process. As shown in Figure 2, we recorded two types of trigger event times for each frame f : $t_{\text{trig,on},f}$ corresponding to the light-side encoder, and $t_{\text{trig,off},f}$ corresponding to the camera-side encoder. These trigger times are utilized in two ways: converting event time to correspondence rotation angle and calculating the dynamic offset

angles between two QWPs. To convert event times to corresponding angles, we used the following relation:

$$\theta = \omega t = \pi \frac{t - t_{\text{trig,on},f}}{t_{\text{trig,on},f+1} - t_{\text{trig,on},f}}. \quad (6)$$

The dynamic offset angles between the two QWPs are calculated as follows:

$$\phi_{\text{dynamic},f} = \pi \frac{t_{\text{trig,on},f} - t_{\text{trig,off},f}}{t_{\text{trig,on},f+1} - t_{\text{trig,on},f}}. \quad (7)$$

These calculations ensure the alignment of rotation angles with event times on independently rotated motors.

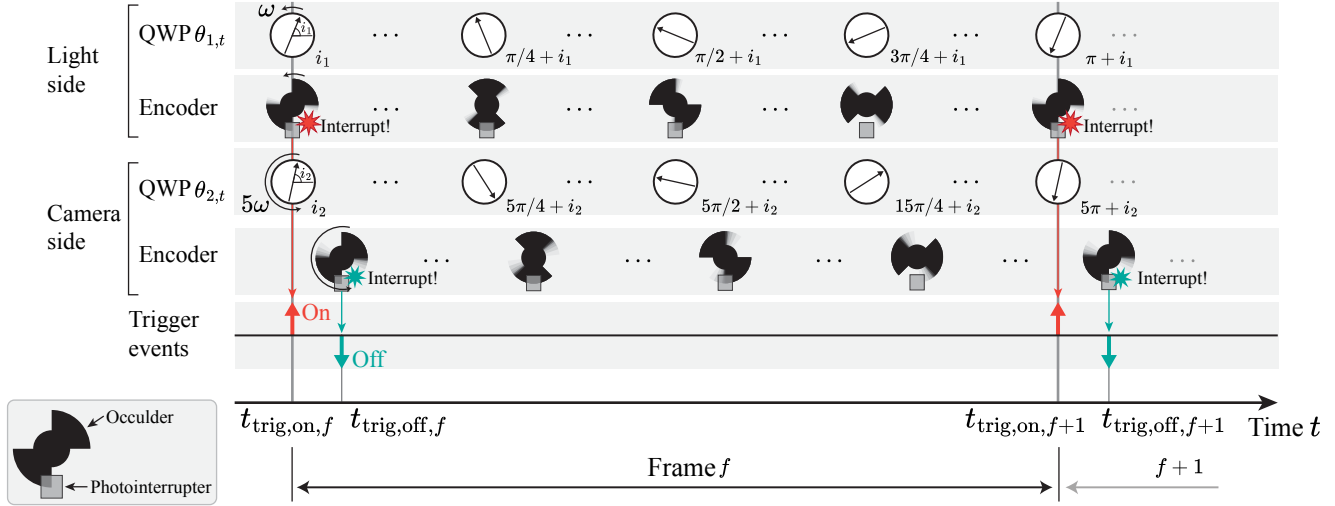


Figure 2. Timeline of motor rotation and trigger events.

3.4. Contrast Threshold Calibration

We calibrate the contrast threshold C using the events observed under controlled illumination stimuli. As shown in Figure 3(a), the event camera directly faced the LED light. The light intensity was modulated using an LED driver (Thorlabs DC2200) and a function generator (Digilent Analog Discovery 3), which also provided a synchronization trigger to align event timings with modulation. We employ the linearly increasing/decreasing function to modulate the intensity as follows:

$$I_t = at + b, \quad (8)$$

where a is coefficient of slope, and b is initial intensity of light. Figure 3(b) shows the electronic current to LED in our calibration. The derivative of the logarithmic intensity under this stimulus is given by:

$$\frac{\partial \log I_t}{\partial t} = \frac{\frac{\partial I_t}{\partial t}}{I_t} = \frac{a}{at + b}. \quad (9)$$

This establishes a linear relationship between t and Δt as follows

$$\frac{pC}{\Delta t} = \frac{a}{at + b} \quad (10)$$

$$\Rightarrow \Delta t = pC \left(t + \frac{b}{a} \right). \quad (11)$$

Using this equation, we can calibrate the contrast threshold C by linear regression with respect to t and Δt .

Calibration was performed for both "on" and "off" events for each pixel. To reduce noise, measurements were repeated 15 times, and all events were used. Additionally, to avoid saturation due to an excessive number of events, we restricted the region of interest (ROI) to 80×80 pixels, with the ROI scanned across the entire pixel array. Figure 3(c) shows the fitted result on one pixel.

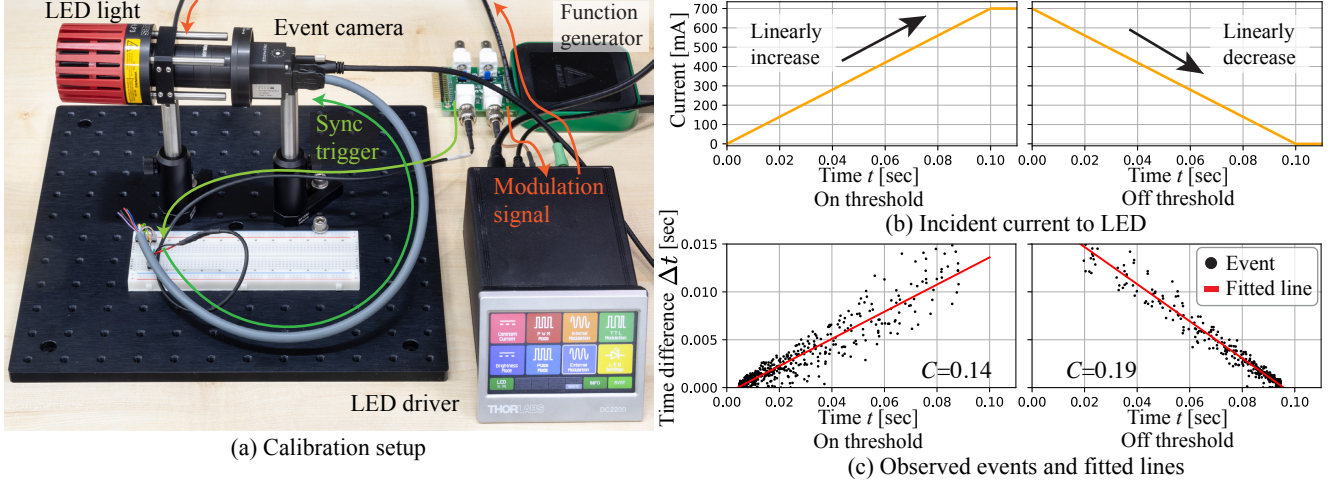


Figure 3. Calibration of contrast threshold. (a) Calibration setup. (b) We linearly increase/decrease the incident current to the LED, and the light intensity is proportionally modulated by the amount of current. (c) From observed events, we fit the linear equation and get the per-pixel contrast threshold for both on and off events. This figure shows one example of a fitted result resulting in $C=0.14$ for on events and $C=0.19$ for off events.

3.5. QWP Offset Angle Calibration

We calibrate the offset angles of the fast axis of the QWP, denoted as ϕ_{calib1} and ϕ_{calib2} (see Equation (4) and (5)). These offsets arise during the attachment of the QWP and the occluder to the motor's shaft. To calibrate these angles, we measure the events of a QWP as a known reference target, as shown in Figure 4(a). Unlike air or a linear polarizer, the use of a QWP enables the determination of a unique solution. The modulated intensity under this condition is expressed as follows:

$$I_t = [\mathbf{L}(0)\mathbf{Q}(\theta_{2,t})\mathbf{D}(\alpha)\mathbf{Q}(\pi/4)\mathbf{Q}(\theta_{1,t})\mathbf{L}(0)\mathbf{s}]_0, \quad (12)$$

where \mathbf{D} is the Mueller matrix of depolarizer, representing depolarization due to non-ideal optics:

$$\mathbf{D}(\alpha) = \begin{bmatrix} 1 & 0 & 0 & 0 \\ 0 & \alpha & 0 & 0 \\ 0 & 0 & \alpha & 0 \\ 0 & 0 & 0 & \alpha \end{bmatrix}. \quad (13)$$

The parameter α ($0 \leq |\alpha| \leq 1$) is the depolarization factor, with smaller values of α corresponding to greater depolarization. In this calibration, α was set to 0.8.

To find the offset angles, we used the log-derivative form of Equation (12) and performed a grid search to identify the pair of angles that best fit the observed events. Figure 4(b) shows the error map that highlights unique angle combinations.

4. Additional Results

4.1. Ablation Study

In addition to Figure 4(c) in the main paper, we conducted an additional ablation study on real data of air (Figure 5(a)). First, we evaluate the impact of Cloude's filter in the per-pixel reconstruction step. With and without Cloude's filter, the reconstruction error is 0.03697 and 1.12×10^{12} , respectively. This result indicates the strong effectiveness of the filtering step in improving reconstruction accuracy. Second, we assess the impact of propagation and random perturbation, as summarized in Table 2. Combining both methods improves reconstruction performance. Although the effect of random perturbation is relatively subtle, it plays a crucial role in preventing direct value copying from neighboring pixels, thereby enabling more precise optimization.

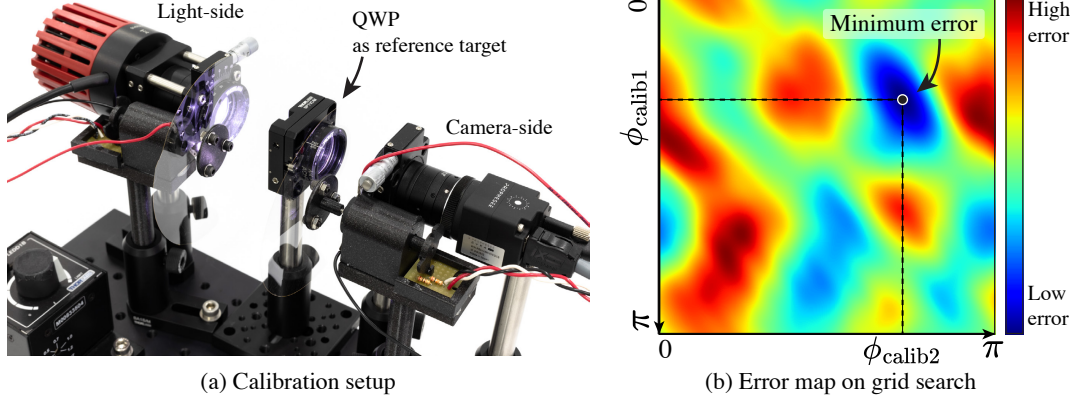


Figure 4. Calibration of QWP offset angles. (a) Calibration setup. We placed the QWP between light and camera in transmission mode. (b) The error map to find the optimal angles with the grid search algorithm. This error map shows the unique solution with the measurement of QWP.

Table 2. Ablation study of propagation and random perturbation with mean squared error (MSE) and mean absolute error (MAE).

Propagation	Perturbation	MSE (\downarrow)	MAE (\downarrow)
–	✓	0.03614	0.12781
✓	–	0.01665	0.08816
✓	✓	0.01661	0.08688

4.2. Rotation Stability of the Prototype

To assess the rotation stability of the motors in our prototype, we recorded the encoder interruption times and subsequently converted them into rotation speeds. Figure 5 shows the measured rotation speeds of the two motors, set to 15Hz and 75Hz, respectively. Both motors achieve stable rotation at their target speeds within three seconds.

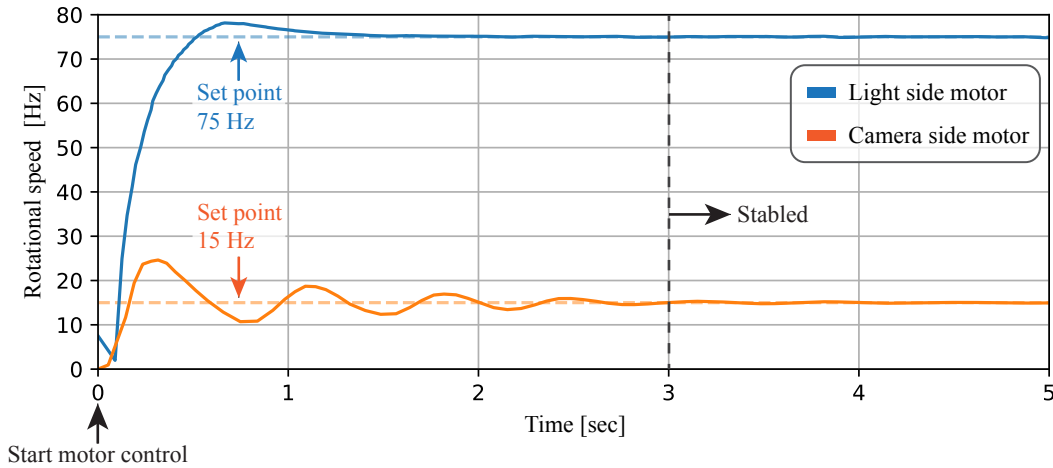


Figure 5. Measured rotation speed of the two motors. The set point is 15 Hz with a standard deviation of 0.31 for the light-side motor and 75 Hz with a standard deviation of 0.07 for the camera-side motor. The rotation speeds stabilize at the set point within three seconds.

Additionally, we examined the temporal stability of Mueller matrix reconstruction. Figure 6 shows the dynamic offset angle $\phi_{\text{dynamic},f}$ and the reconstructed Mueller matrix of LP45° (shown in Figure 5(a)). While slight variations exist due to imperfect synchronization, the reconstructed Mueller matrix remains stable.

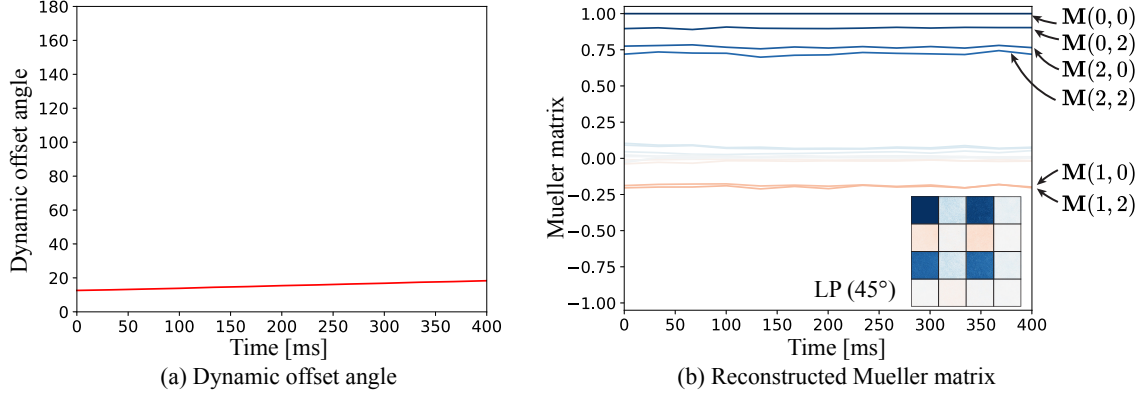


Figure 6. Synchronization and reconstruction stability.

4.3. Comparison with Frame-based Method

We conducted an additional evaluation by comparing our method with a conventional frame-based approach [1] for the metal plate scene (Figure 4(b)). For the frame-based measurement, we captured exposure-bracketed images by changing the exposure times, which were merged into a HDR image. HDR images were captured under 36 combinations of QWP rotation angles, requiring approximately 5 minutes to acquire a single Mueller matrix image. As shown in Figure 7, our event-based method produces results comparable to the frame-based method, validating its accuracy while achieving significantly faster capture times (33 ms). Inevitable differences arise due to various variations, such as camera positioning.

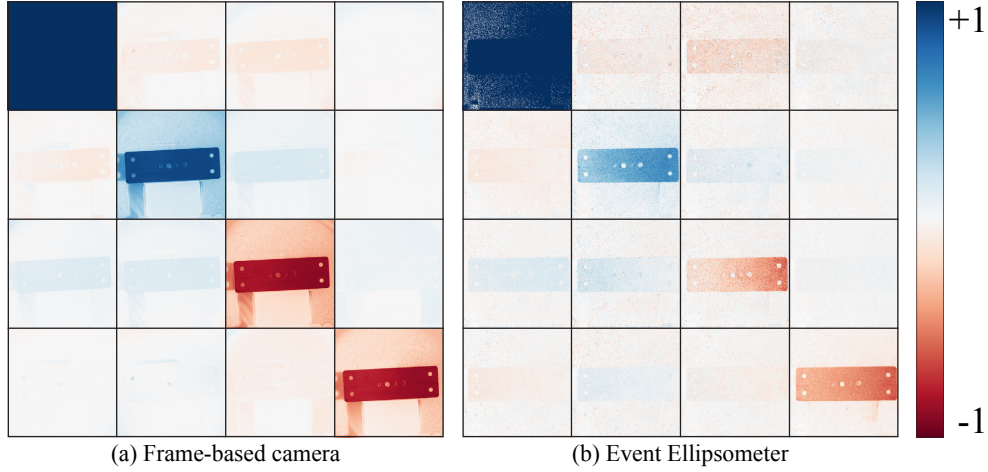


Figure 7. Evaluation with the frame-based method [1] requires 5 min to capture, whereas our approach achieves it in just 33 ms.

4.4. Comparison with Single-shot Method

As shown in Figure 8, we compare our method against a single-shot method [8] using synthetic data. This single-shot method relies on specialized and high-cost nano-phonic metasurfaces, which simultaneously alter both ray positions and directions, as well as polarization states, making the simulation with arbitrary 3D geometry challenging.

To enable a feasible simulation, we simplify the target scene's geometry to a planar surface. With the ideal coaxial setup of the camera and light source, we can ensure exact correspondence between camera pixels and the projection pattern. The reconstructed Mueller matrix image under this ideal setup is shown in Figure 8(a). However, their method exhibits high sensitivity to misalignment under realistic conditions (Figure 8(b)). In contrast, our method (Figure 8(c)) can reconstruct the scene while allowing greater flexibility in light positioning, enhancing practical usability.

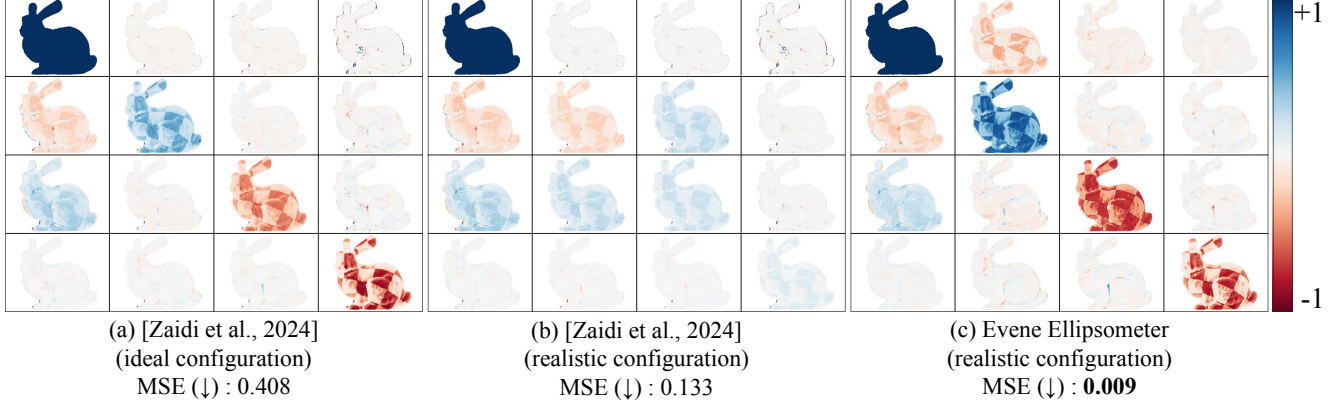


Figure 8. Comparison with the single-shot method [8] using synthetic data.

4.5. Statistics of Event Rate

We computed event rate statistics across all scenes. The minimum, maximum, average, and standard deviation of event rates is 10.3, 171.9, 91.8, and 41.1 MEv/s, respectively. Empirically, we confirmed that stable event capture within this event rate range is achieved by appropriately setting the ROI.

4.6. Detailed Results with Decomposed Mueller Matrix

Figure 9 to 14 show the more detailed result of the reconstructed Mueller matrix in the main paper along with decomposed images that offer deeper insights into the scene. These decompositions are obtained through the Lu-Chipman decomposition method [7], which decomposes the reconstructed Mueller matrix \mathbf{M} into three distinct Mueller matrices:

$$\mathbf{M} = \mathbf{M}_{\Delta} \mathbf{M}_R \mathbf{M}_D. \quad (14)$$

where \mathbf{M}_{Δ} , \mathbf{M}_R and \mathbf{M}_D represent depolarization, retardance, and diattenuation, respectively.

Diattenuation D quantifies the magnitude of reflection/transmission of polarized light and is defined as:

$$D = \frac{1}{\mathbf{M}_{00}} \sqrt{\mathbf{M}_{01}^2 + \mathbf{M}_{02}^2 + \mathbf{M}_{03}^2} \quad (15)$$

Polarizance P quantifies the magnitude of unpolarized light that becomes polarized after reflection/transmission as follows:

$$P = \frac{1}{\mathbf{M}_{00}} \sqrt{\mathbf{M}_{10}^2 + \mathbf{M}_{20}^2 + \mathbf{M}_{30}^2} \quad (16)$$

Polarization preservation ρ shows the preservation magnitude of the polarized incident as follows:

$$\rho = \frac{1}{3} (\mathbf{M}_{\Delta,11} + \mathbf{M}_{\Delta,20} + \mathbf{M}_{\Delta,11}) \quad (17)$$

where higher ρ values are typically associated with specular reflection components.

Retardance R represents the phase shift introduced by retarder components and is given by:

$$R = \cos^{-1} \left(\frac{\text{tr}(\mathbf{M}_R)}{2} - 1 \right) \quad (18)$$

where $\text{tr}(\cdot)$ denotes the trace operator. To enhance the visualization of this phase information, we modulate the retardance with polarization preservation values, highlighting regions with notable polarization effects.

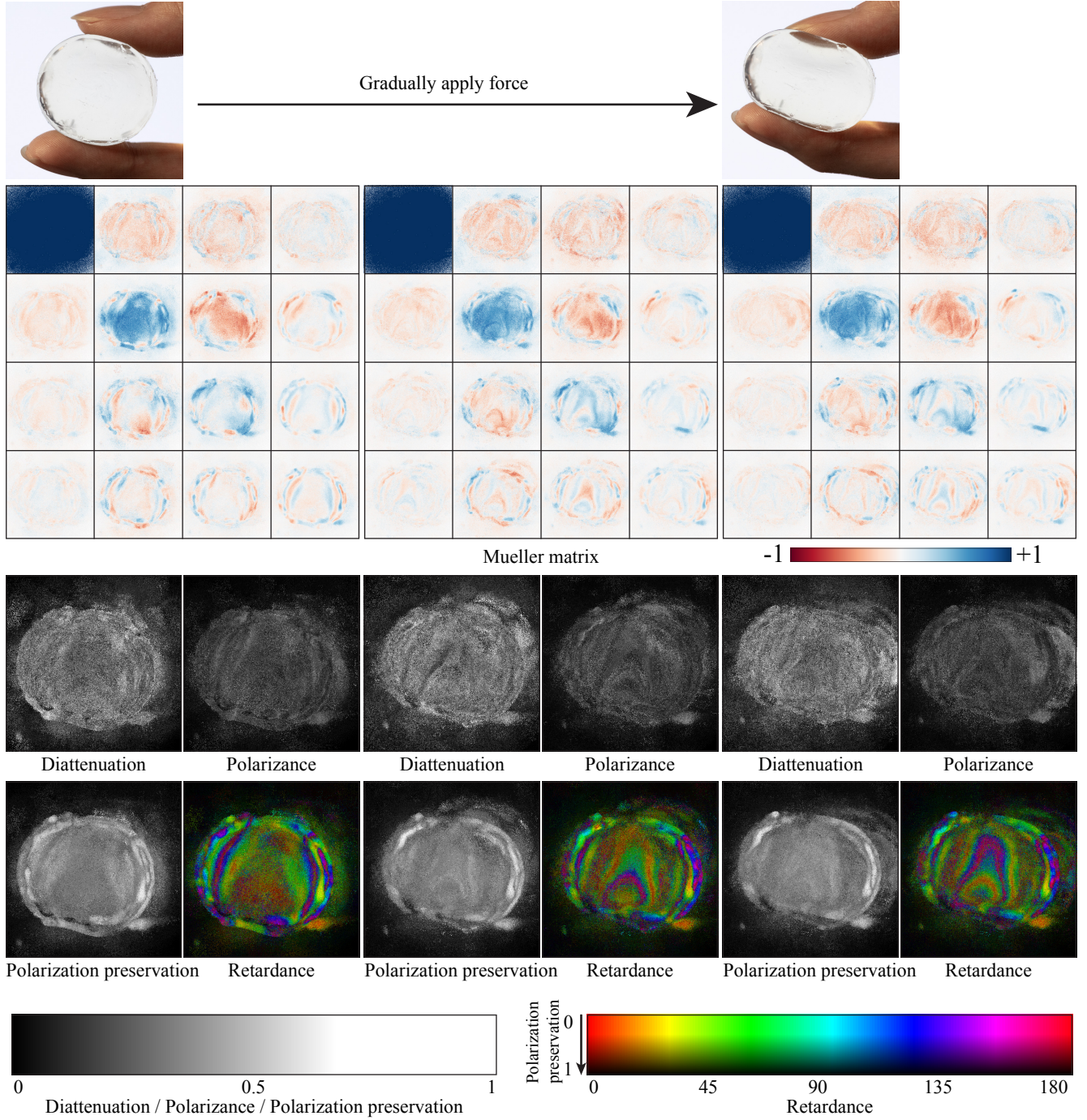


Figure 9. Detailed visualization of Mueller matrix of the photoelasticity analysis scene. The ROI is 500×500 , and the average event rate is 151.7 MEv/s.

5. Additional Discussion

5.1. Wavelength Dependency

Our prototype utilizes a white LED light source and a monochrome event camera, which captures a mixture of visible wavelengths. However, polarization states are wavelength-dependent, introducing potential inaccuracies. For instance, the

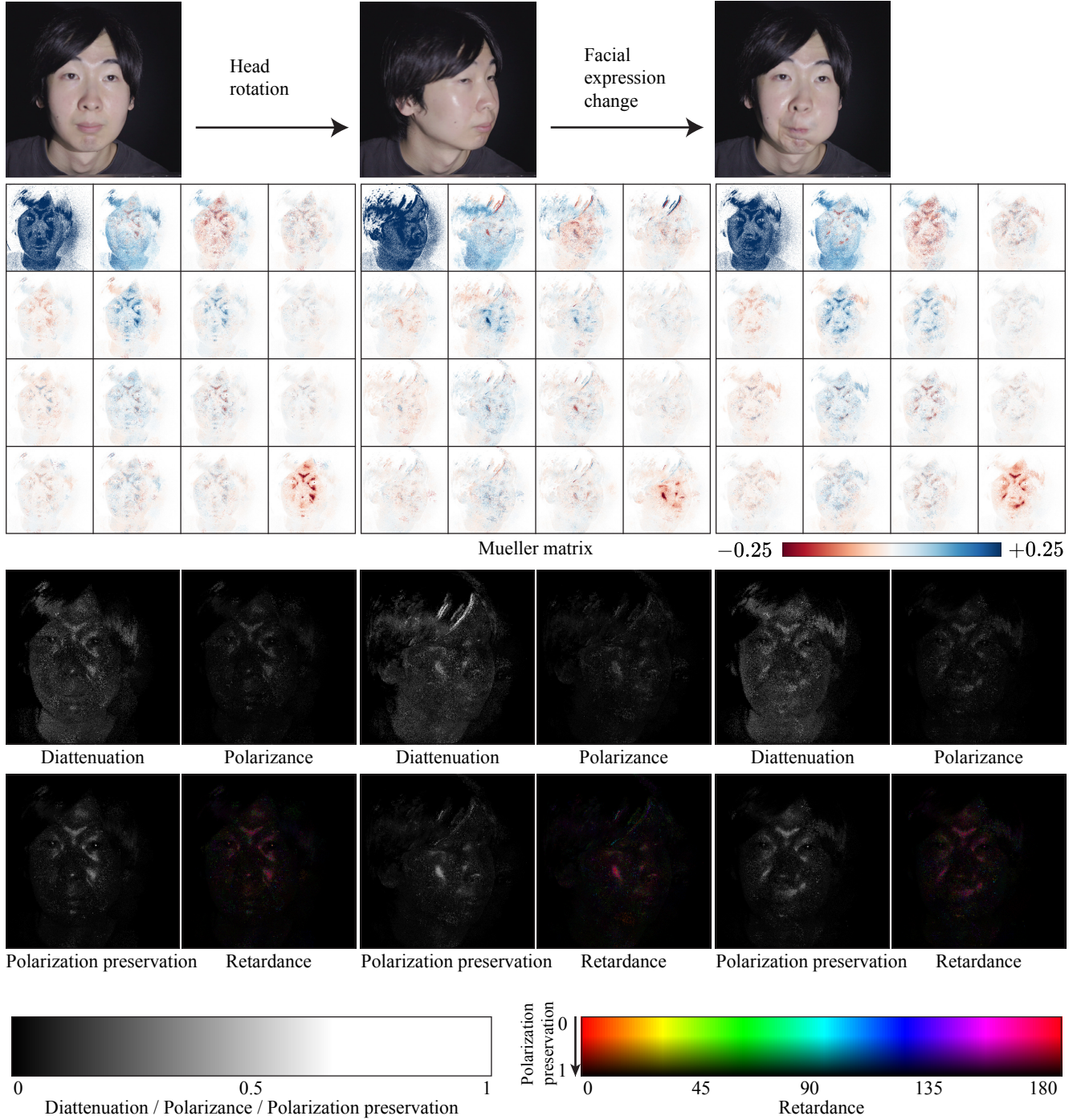


Figure 10. Detailed visualization of Mueller matrix of the face scene. The ROI is 600×600 , and the average event rate is 26.6 MEv/s.

QWP exhibits slight wavelength-dependent variations in retardance, and the reflection/transmission properties of the scene can also differ across wavelengths [5]. To address this issue, a bandpass filter with the desired wavelength can be attached in front of the camera. This filter restricts light to a single wavelength, mitigating the wavelength dependency. However, this approach reduces the overall light intensity, potentially leading to a non-ideal response from the event sensor [3, 6].

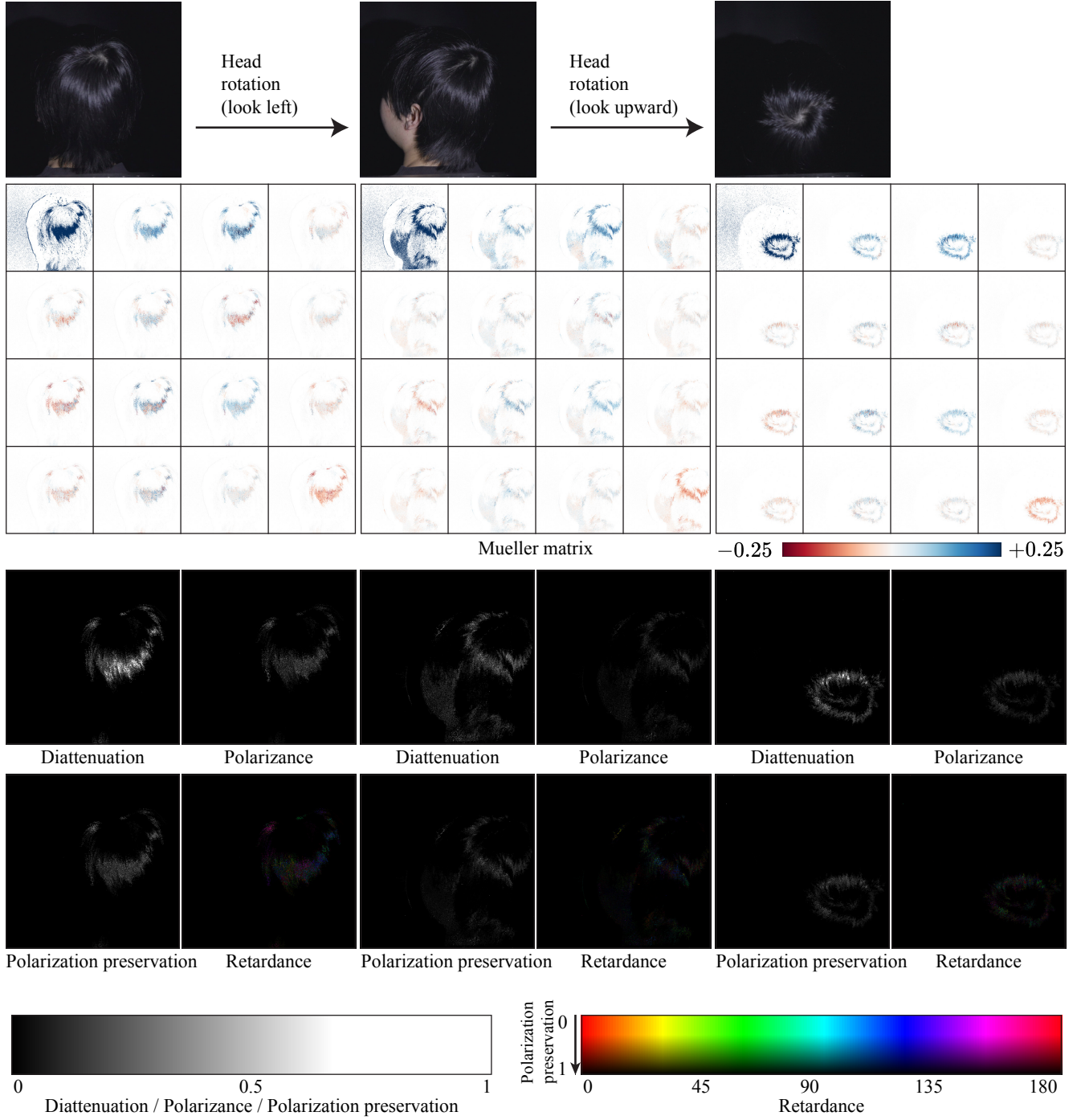


Figure 11. Detailed visualization of Mueller matrix of the hair scene. The ROI is 600×600 , and the average event rate is 10.3 MEv/s.

5.2. Temporal Artifact in the Mueller-matrix Video

The reconstructed Mueller matrix video exhibits frame-to-frame temporal artifacts. These artifacts are primarily caused by reflections on the QWP films due to the lack of adequate anti-reflection coatings and the presence of fine dust on the surface. Furthermore, the thin QWP films tend to fluctuate during rotation, causing variations in their surface normals and introducing temporal artifacts.

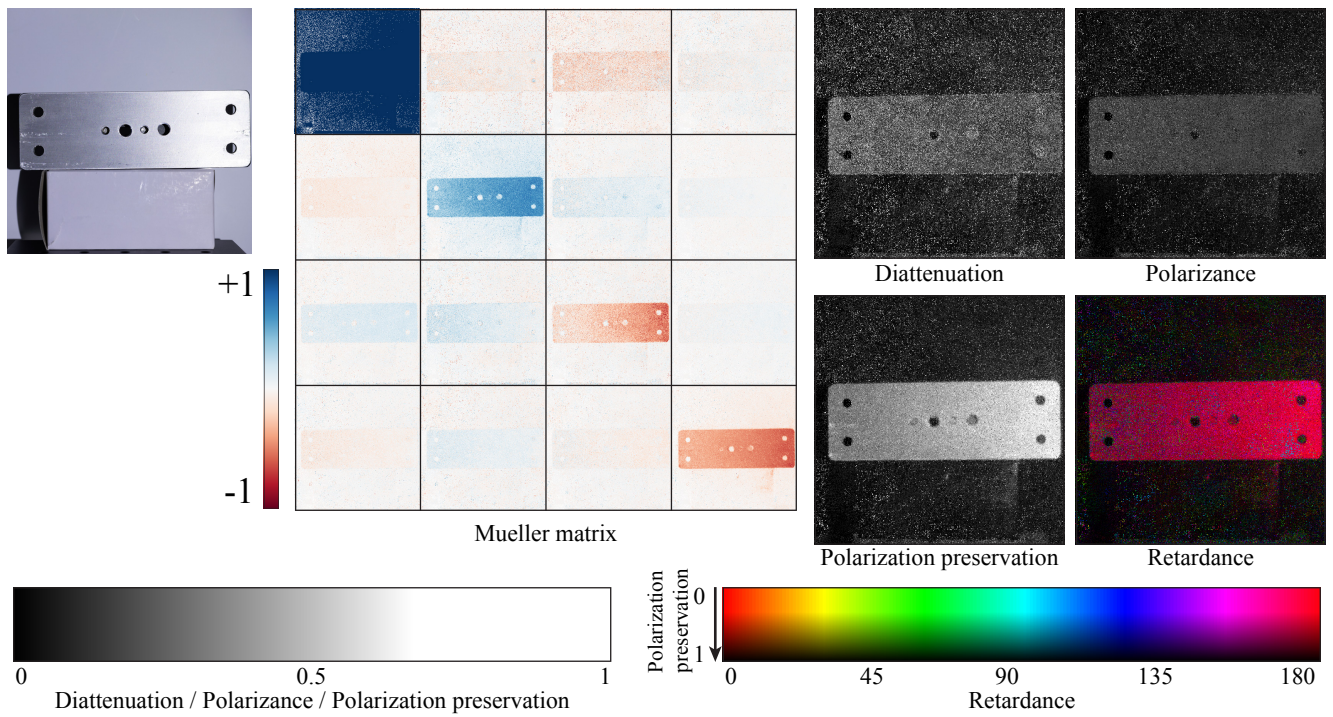


Figure 12. Detailed visualization of Mueller matrix of the metal plate scene. The ROI is 400×400 , and the average event rate is 110.4 MEV/s.

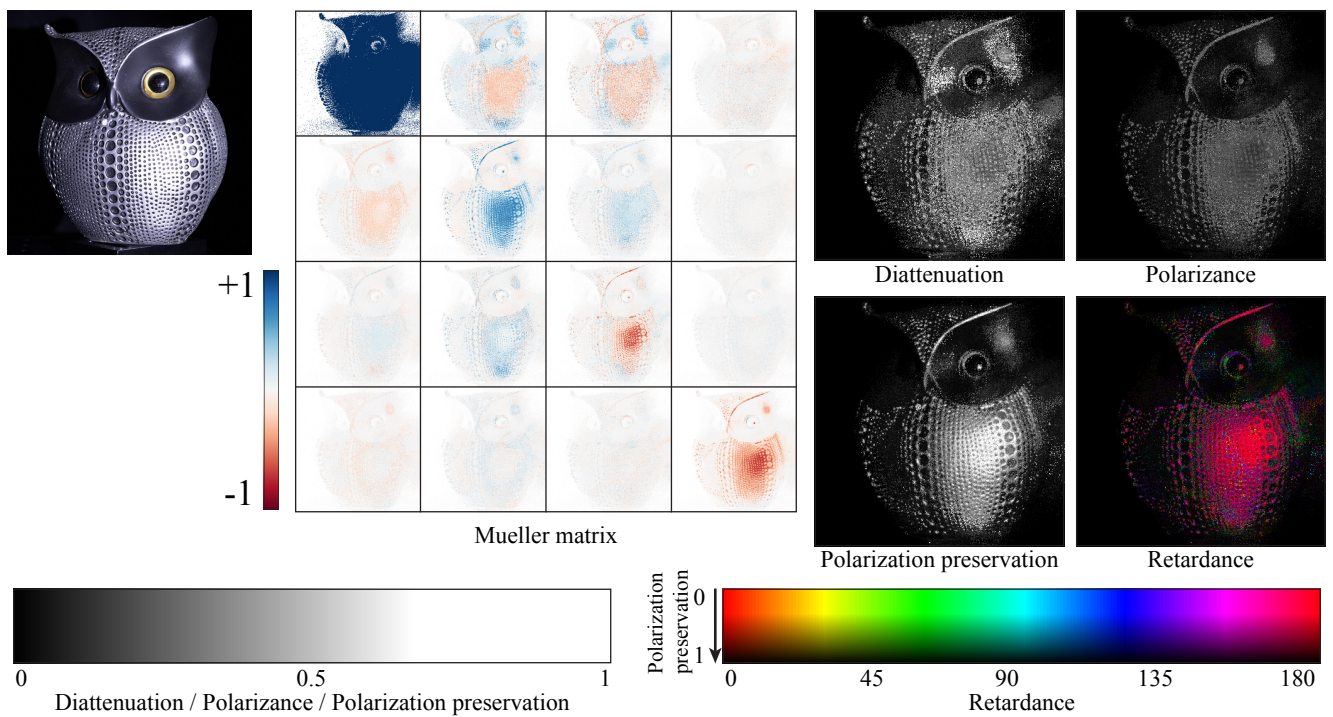


Figure 13. Detailed visualization of Mueller matrix of the owl statue scene. The ROI is 400×400 , and the average event rate is 62.7 MEV/s.

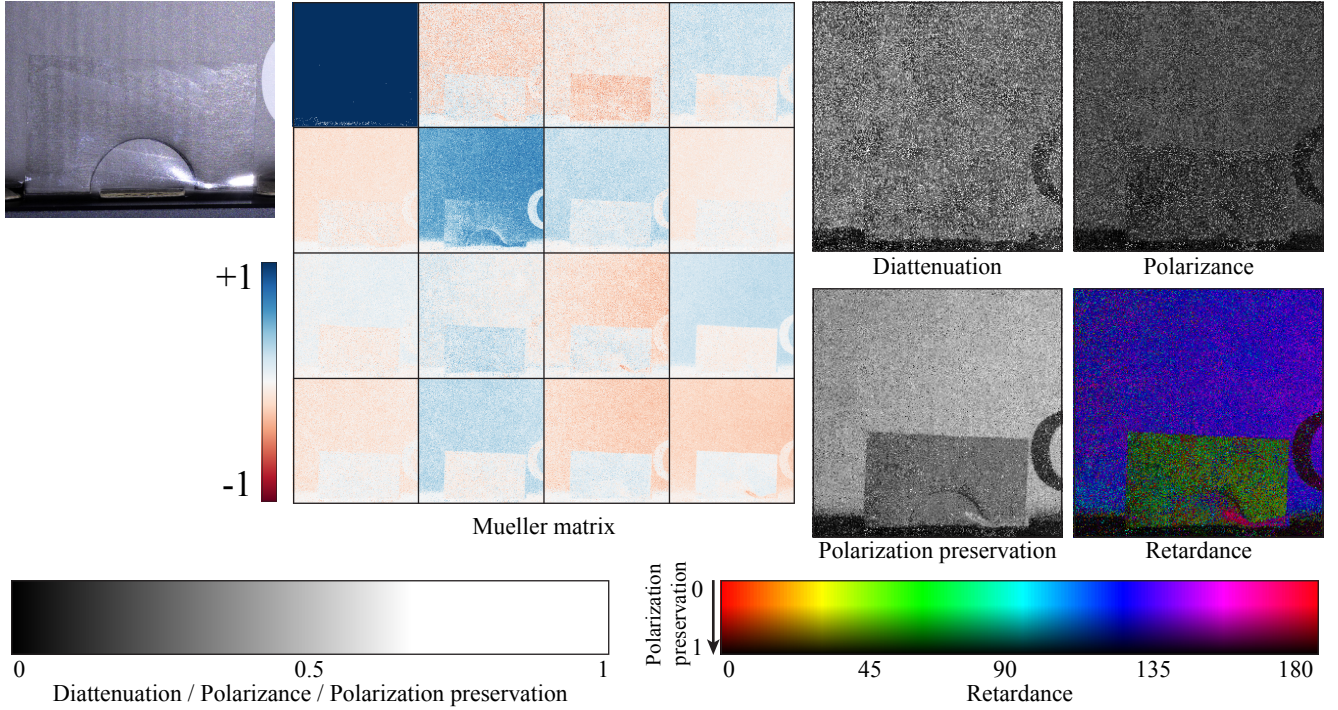


Figure 14. Detailed visualization of Mueller matrix of the tape scene. The ROI is 256×256 , and the average event rate is 74.4 MEV/s.

5.3. Motion Artifacts

Our method assumes that small motions within a single frame are negligible. However, reconstruction accuracy may degrade when event generation is dominated by object motion rather than polarization-induced changes. We observed such motion artifacts in the human hair scene (Figure 11). Specifically, the dark regions of human hair rarely produce polarization-triggered events, making it challenging to accurately reconstruct the Mueller matrix. Addressing these limitations remains a topic for future work.

5.4. Motor Selection

In our hardware prototype, we utilized brushed DC motors, though alternative motor types could be considered. The brushed DC motor is affordable and offers high rotation speed under light load conditions. However, synchronizing two brushed DC motors precisely at high rotation speeds is difficult. We addressed this problem by independently controlling the rotation speed (Section 3.2) and compensating for the phase difference between two motors using encoder signals (Section 3.3). For faster rotation speed and more precise control, a brushless DC motor, also known as an electronically commutated (EC) motor, presents a viable alternative. EC motors provide precise control at high speed, potentially simplifying the hardware system and improving rotation stability. However, EC motors are generally more expensive than brushed motors.

References

- [1] Seung-Hwan Baek, Tizian Zeltner, Hyunjin Ku, Inseung Hwang, Xin Tong, Wenzel Jakob, and Min H Kim. Image-based acquisition and modeling of polarimetric reflectance. *ACM Trans. Graph.*, 39(4):139, 2020. 7
- [2] Edward Collett. Field guide to polarization. Spie Bellingham, 2005. 2
- [3] Guillermo Gallego, Tobi Delbrück, Garrick Orchard, Chiara Bartolozzi, Brian Taba, Andrea Censi, Stefan Leutenegger, Andrew J Davison, Jörg Conradt, Kostas Daniilidis, et al. Event-based vision: A survey. *IEEE transactions on pattern analysis and machine intelligence*, 44(1):154–180, 2020. 10
- [4] Silvano Galliani, Katrin Lasinger, and Konrad Schindler. Massively parallel multiview stereopsis by surface normal diffusion. In *Proceedings of the IEEE international conference on computer vision*, pages 873–881, 2015. 2, 3
- [5] Yujin Jeon, Eunsue Choi, Youngchan Kim, Yunseong Moon, Khalid Omer, Felix Heide, and Seung-Hwan Baek. Spectral and polar-

ization vision: Spectro-polarimetric real-world dataset. In *Proceedings of the IEEE/CVF Conference on Computer Vision and Pattern Recognition*, pages 22098–22108, 2024. 10

- [6] Haoyue Liu, Shihan Peng, Lin Zhu, Yi Chang, Hanyu Zhou, and Luxin Yan. Seeing motion at nighttime with an event camera. In *Proceedings of the IEEE/CVF Conference on Computer Vision and Pattern Recognition*, pages 25648–25658, 2024. 10
- [7] Shih-Yau Lu and Russell A Chipman. Interpretation of mueller matrices based on polar decomposition. *JOSA A*, 13(5):1106–1113, 1996. 8
- [8] Aun Zaidi, Noah A Rubin, Maryna L Meretska, Lisa W Li, Ahmed H Dorrah, Joon-Suh Park, and Federico Capasso. Metasurface-enabled single-shot and complete mueller matrix imaging. *Nature Photonics*, pages 1–9, 2024. 7, 8